Embedded fibre Bragg grating sensors for non-uniform strain sensing in composite structures

Hang-yin Ling[1], Kin-tak Lau[1], Li Cheng[1] and Kwok-wing Chow[2]

[1] Department of Mechanical Engineering, The Hong Kong Polytechnic University, Hong Kong, People's Republic of China
[2] Department of Mechanical Engineering, The University of Hong Kong, Hong Kong, People's Republic of China

E-mail: carrie.lhy@polyu.edu.hk

Abstract
A methodology for evaluating the response of embedded fibre Bragg grating (FBG) sensors in composite structures based on the strain in a host material is introduced. In applications of embedded FBG sensors as strain sensing devices, it is generally assumed that the strain experienced in a fibre core is the same as the one measured in the host material. The FBG sensor is usually calibrated by a strain gauge through a tensile test, centred on obtaining the relationship between the surface strain in the host material and the corresponding Bragg wavelength shift obtained from the FBG sensor. However, such a calibration result can only be valid for uniform strain measurement. When the strain distribution along a grating is non-uniform, average strain measured by the strain gauge cannot truly reflect the in-fibre strain of the FBG sensor. Indeed, the peak in the reflection spectrum becomes broad, may even split into multiple peaks, in sharp contrast with a single sharp peak found in the case of the uniform strain measurement. In this paper, a strain transfer mechanism of optical fibre embedded composite structure is employed to estimate the non-uniform strain distribution in the fibre core. This in-fibre strain distribution is then utilized to simulate the response of the FBG sensor based on a transfer-matrix formulation. Validation of the proposed method is preceded by comparing the reflection spectra obtained from the simulations with those obtained from experiments.

Keywords: fibre Bragg grating (FBG) sensors, strain measurement, transfer matrix, non-uniform strain

(Some figures in this article are in colour only in the electronic version)

1. Introduction

Fibre Bragg grating (FBG) sensors have been exploited as intrinsic strain sensors for the applications of smart composite structures in aerospace, marine and civil engineering communities over the past decades due to their superior characteristics such as localized strain measurement ability, relatively small size, high sensitivity, inertness to electric or magnetic inference and multiplexing capability [1, 2]. The

FBG sensors are most commonly used as point sensors to measure an average strain over their gauge length by examining the Bragg wavelength shift in a reflection spectrum. On the other hand, they can also be capable of the determination of a distributed strain field along the grating [3].

For strain sensing applications, a bare optical fibre is usually surrounded by a protective coating in order to avoid the defects induced in the optical fibre during the fabrication process of a smart composite. The presence of the protective

coating influences the strain transfer efficiency from a host material to an embedded FBG sensor. Moreover, the precision of strain measurement in the embedded FBG sensor depends mainly on the bonding characteristics of a fibre core, the protective coating, an adhesive layer and the host material. In general, the strain measured in the fibre core is assumed to be equivalent to the one experienced by the host material [4]. However, the strain experienced by the host material is not totally transferred to the bare fibre as part of the energy is absorbed by the protective coating and the adhesive layer when the structure is loaded. To measure the actual strain in the fibre core, the aspect of strain transfer mechanism of optical fibre embedded composite structure has been considered [5–7]. Duck and LeBlanc [6] investigated the mechanical load transfer from a fibre core to a host material by theoretical approaches. In their studies, the effects generated by the thickness of a protective coating and an adhesive layer were neglected. With a known strain field of the host material, an in-fibre strain profile along the fibre core can be estimated. It was found that the strain transfer efficiency is highly dependent on the variation of the strain field in the host material. Subsequently, Lau *et al* [7] proposed a theoretical model to interpret the effects induced by the adhesive thickness and the protective coating material on embedded FBG sensors. An axial strain profile in a fibre core can be calculated provided that an axial strain of a host material at the mid-span of the beam is known.

A calibration test is widely used in establishing the relationship between the strain in the host material and the response of the FBG sensor, in which the Bragg wavelength shift is obtained from the reflection spectrum and the strain variation is recorded by using a strain gauge [8]. Although such a reflection spectrum can quantitatively evaluate the uniform strain, the strain distribution along the grating cannot be found. In order to correlate the non-uniform strain distribution along the grating and the reflection spectrum, Huang *et al* [9] applied a transfer-matrix (T-matrix) method, introduced by Tamada and Sakuda [10], to establish the relationship between the applied strain along the grating and the reflection spectrum. This method is broadly accepted for constructing the reflection spectrum from the FBG sensors subjected to a known strain field [3, 11, 12].

Motivated by the necessity of relating the non-uniform strain in the host material and the form of the reflection spectrum from the embedded FBG sensors, this paper presents a methodology for evaluating the response of the embedded FBG sensors in the composite structures based on the surface strain of the host material. Evaluation of the non-uniform strain measurement of the FBG sensor is carried out on the basis of a strain transfer mechanism of an optical fibre embedded composite structure, a finite-element model (FEM) and a transfer-matrix (T-matrix) formulation. Firstly, the strain distribution of the host material subjected to a bending load is numerically calculated by the FEM. Then, the strain transfer mechanism is employed for obtaining the in-fibre strain distribution of the embedded FBG sensor. Lastly, such a strain distribution is utilized to simulate the FBG sensor response based on the T-matrix formulation. The proposed method for the in-fibre non-uniform strain evaluation is validated by comparing the reflection spectra obtained from the simulations with those obtained from experiments.
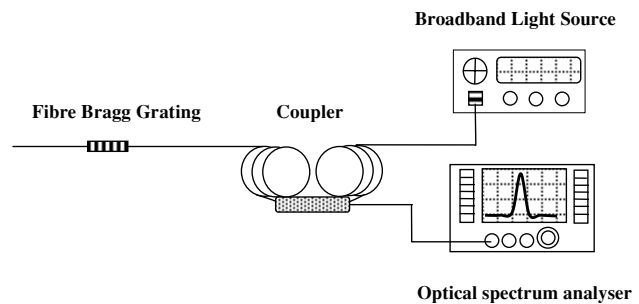
Figure 1. A typical FBG measuring system.

2. Non-uniform strain sensing principle of the FBG sensor

A FBG, in which a spatially periodic modulation has been imposed on the refractive index of the core of a single mode fibre, is fabricated by exposing a segment of the fibre to an interference pattern of ultraviolet light. The length of the FBG normally varies from 1 to 20 mm for meeting versatile sensing purposes and the grating reflectivity can be approximately 100% in an ideal case [13]. A typical FBG measuring system, shown in figure 1, consists of a FBG sensor, a broadband light source, a 3 dB fibre optic coupler and an optical spectrum analyser (OSA). Light is emitted from the broadband light source to the FBG sensor via the coupler. Similar to a Y-type channel, the role of the coupler is to guide the emitted light to the FBG sensor and the reflective signals back to the OSA simultaneously. The reflective signals from the FBG sensor are then recorded by the OSA in which the reflection spectrum with a sharp single peak is observed as a result.

The FBG sensor, prepared for processing embedment, is always formed by three different cylindrical layers which are the fibre core, a cladding and the protective coating. Figure 2 depicts the configuration and the light propagation in the FBG sensor. Generally, the fibre core is surrounded by the cladding which is made of silica glass, and both fibre core and coating have the same mechanical properties. The protective coating is the outermost layer of the sensor for protecting the fibre from damage and moisture absorption. According to Bragg's law, the Bragg wavelength (λ_B) that is reflected from the sensor is given by

$$\lambda_B = 2n_B\Lambda, \tag{1}$$

where Λ is the spacing between maxima in index modulation, the so-called 'spatial pitch', and n_B is the refractive index of the fibre core. Both the spatial pitch and the refractive index are dependent on the strain and the temperature that the FBG exposes.

Unlike a uniform strain sensing, where both spatial pitch and refractive index of the fibre core proportionally change along the grating, non-uniform strain causes non-uniform variation of the spatial pitch and the refractive index of the fibre core along the grating. For a grating subjected to a non-uniform strain, $\varepsilon_{xx}(x)$, along the longitudinal direction (x-direction), equation (1) can be rewritten as

$$\lambda_B(x) = 2n_{eff}(x)\Lambda(x) = 2n_{eff0}\Lambda_0[1 + a\varepsilon_{xx}(x)], \tag{2}$$

where $a = 1 - \frac{1}{2}n_0^2[p_{12} - \nu(p_{11} - p_{12})]$ is the grating gauge factor [14], in which p_{11} and p_{12} are the strain-optic constants
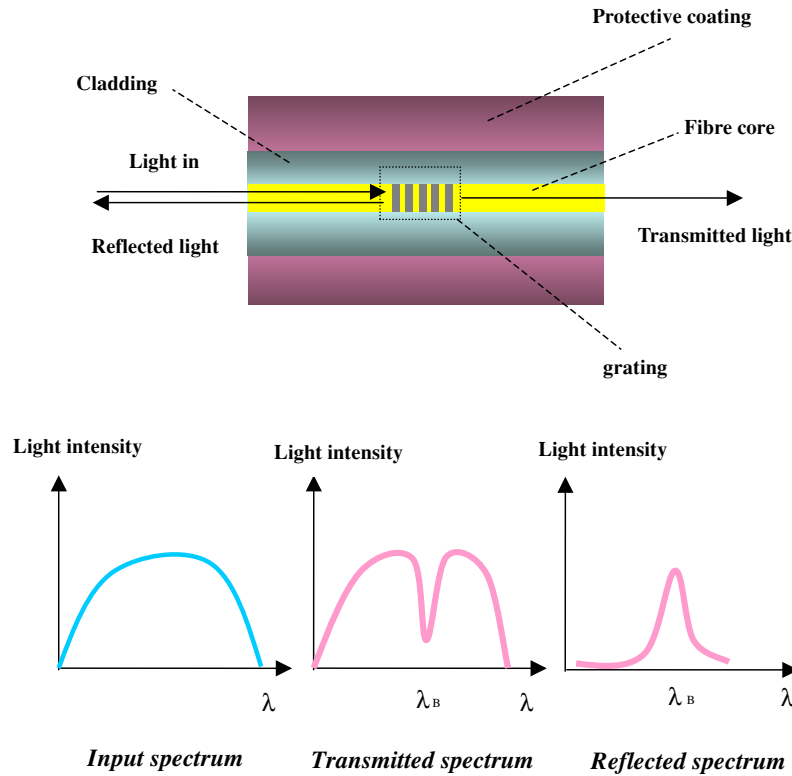
Figure 2. Configuration and light propagation in the FBG sensor.

for the optical fibre and ν is Poisson's ratio. Λ_0 and n_{eff0} are the initial spatial pitch and the initial refractive index of the fibre core at the strain-free state, respectively. Equation (2) implies that the Bragg wavelength varies with the non-uniform strain and results in the deformation of the reflection spectrum.

3. Non-uniform strain sensing

In accordance with the non-uniform strain sensing principle, the reflection spectrum shows a strong correlation with the in-fibre strain distribution along the grating. With the goal of relating the reflection spectrum to the strain distribution of a host material, a strain transfer mechanism is considered. The proposed non-uniform strain evaluating methodology is illustrated by means of the strain transfer mechanism, FEM and T-matrix formulation. By modelling the host material under a three-point bending configuration with the FEM, the surface strain distribution of the host material is numerically calculated. This strain distribution is then transferred to the corresponding in-fibre strain distribution of the embedded FBG sensor through the strain transfer mechanism. It is recalled that this methodology only works for the host with well-understood mechanical properties. As a result, the response of the embedded FBG sensor can be simulated using the T-matrix formulation. The validation of the proposed method for the in-fibre non-uniform strain evaluation can be preceded by means of a comparison of the reflection spectra obtained from the simulations with those obtained from experiments.

3.1. Strain transfer in embedded optical fibre

In Duck and LeBlanc's theoretical model, they only considered a two-cylinder model to represent the strain transfer mechanism between the host material and the optical fibre [6]. It was assumed that the optical fibre sensor is modelled as an infinitely long axisymmetric system and both host material and optical fibre are isotropic. From a practical point of view, this model cannot represent the situation of the composite structure with embedded optical fibre sensor, since the optical fibre sensor always includes the protective coating which protects the bare optical fibre from damage during the embedment process. As a result, a four-cylinder model considered by one of the authors is studied here [7]. In the consideration of the bonding characterization at the interfaces between the host material and the adhesive layer, the adhesive layer and the protective coating, and the protective coating and the fibre core, a modified four-cylinder model shown in figures 3 and 4 is introduced to study the strain transfer of optical fibre embedded composite structure.

In figure 3, the longitudinal direction (z) and the transverse direction (r) represent the direction of the applied load and the distance measured from the centre of the fibre core, respectively. The subscripts f, c, a and m denote the fibre core, protective coating, adhesive layer and host material, respectively. Tensile and shear moduli are given by E and G. $\bar{\sigma}_z$ and τ_{rz} are the mean normal stress acting on the cross section and the shear stress acting on the outer surface of different materials, respectively. The symbols r_f, r_c, r_a and r_m represent the outer radii of the fibre core, protective coating, adhesive layer and host material, respectively, measured from
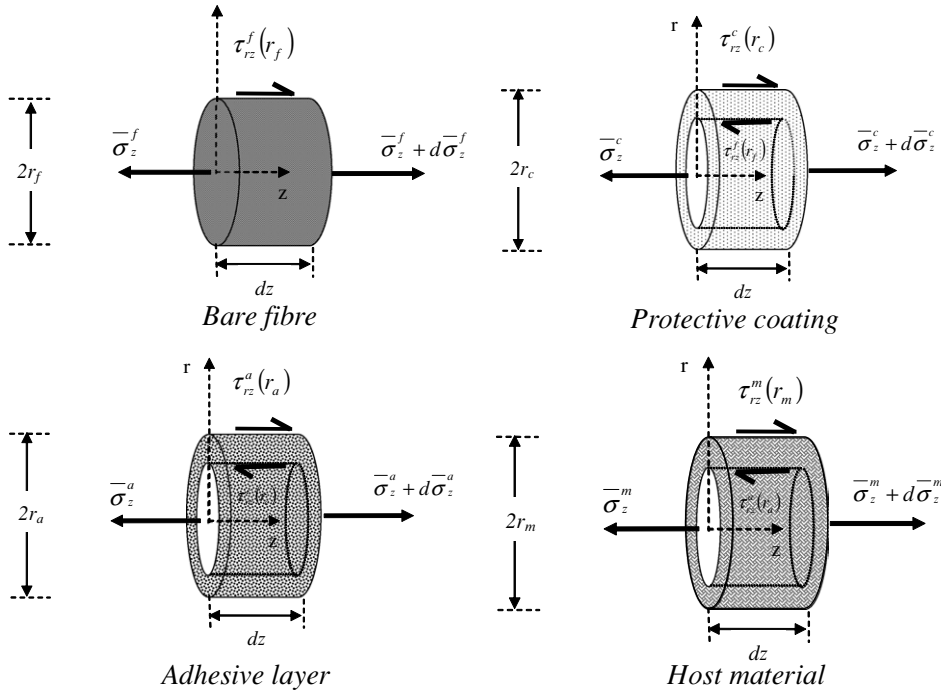
Figure 3. Free-body diagrams of (*a*) bare fibre, (*b*) protective coating, (*c*) adhesive layer and (*d*) host material.
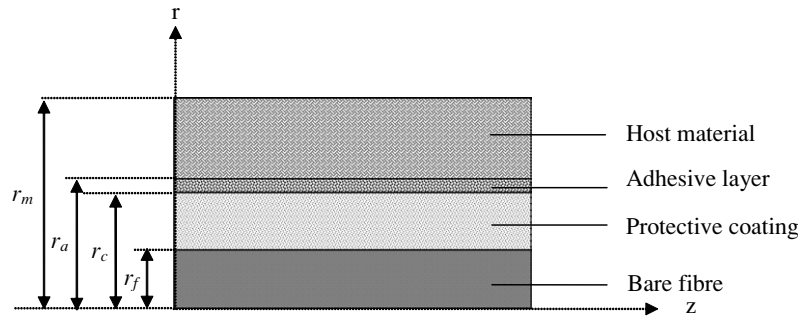
Figure 4. Cross-sectional view of the modified four-cylinder model.

the centre of the fibre core. All basic assumptions are made based on the model presented earlier in the literature [7].

Figure 3 sketches schematic free-body diagrams of an incremental element of different parts of the optical fibre embedded composite system. The force equilibrium equations for the fibre core, protective coating, adhesive layer and host material are expressed as equations (3*a*)–(3*d*), respectively,

$$\frac{\partial \bar{\sigma}_z^{\mathrm{f}}(z)}{\partial z} = \frac{-2\tau_{rz}^{\mathrm{f}}(r_{\mathrm{f}}, z)}{r_{\mathrm{f}}}, \tag{3a}$$

$$\frac{\partial \bar{\sigma}_z^{\mathrm{c}}(z)}{\partial z} \cdot \frac{r_{\mathrm{c}}^2 - r_{\mathrm{f}}^2}{2} = \tau_{rz}^{\mathrm{c}}(r_{\mathrm{f}}, z)r_{\mathrm{f}} - \tau_{rz}^{\mathrm{c}}(r_{\mathrm{c}}, z)r_{\mathrm{c}}, \tag{3b}$$

$$\frac{\partial \bar{\sigma}_z^{\mathrm{a}}(z)}{\partial z} \cdot \frac{r_{\mathrm{a}}^2 - r_{\mathrm{c}}^2}{2} = \tau_{rz}^{\mathrm{a}}(r_{\mathrm{c}}, z)r_{\mathrm{c}} - \tau_{rz}^{\mathrm{a}}(r_{\mathrm{a}}, z)r_{\mathrm{a}}, \tag{3c}$$

$$\frac{\partial \bar{\sigma}_z^{\mathrm{m}}(z)}{\partial z} \cdot \frac{r^2 - r_{\mathrm{a}}^2}{2} = \tau_{rz}^{\mathrm{m}}(r_{\mathrm{a}}, z)r_{\mathrm{a}} - \tau_{rz}^{\mathrm{m}}(r, z)r. \tag{3d}$$

Equations (3*a*) and (3*b*), equations (3*b*) and (3*c*), and equations (3*c*) and (3*d*) are related through the equivalence of shear forces for the bonding characterization at the interfaces between the fibre core and the protective coating, the protective

coating and the adhesive layer, and the adhesive layer and the host material, respectively, i.e., $\tau_{rz}^{\mathrm{f}}(r_{\mathrm{f}}, z) = \tau_{rz}^{\mathrm{c}}(r_{\mathrm{f}}, z)$, $\tau_{rz}^{\mathrm{c}}(r_{\mathrm{c}}, z) = \tau_{rz}^{\mathrm{a}}(r_{\mathrm{c}}, z)$ and $\tau_{rz}^{\mathrm{a}}(r_{\mathrm{a}}, z) = \tau_{rz}^{\mathrm{m}}(r_{\mathrm{a}}, z)$. Therefore, the interfacial shear can be eliminated. By combining equations (3*a*)–(3*d*),

$$\tau_{rz}^{\mathrm{m}}(r, z) = -\frac{E_{\mathrm{f}} r_{\mathrm{f}}^2}{2r} \left[\frac{E_{\mathrm{m}}(r^2 - r_{\mathrm{a}}^2)}{E_{\mathrm{f}} r_{\mathrm{f}}^2} \cdot \frac{\partial \bar{\varepsilon}_z^{\mathrm{m}}(z)}{\partial z} + \frac{E_{\mathrm{a}}(r_{\mathrm{a}}^2 - r_{\mathrm{c}}^2)}{E_{\mathrm{f}} r_{\mathrm{f}}^2} \right.$$
$$\left. \cdot \frac{\partial \bar{\varepsilon}_z^{\mathrm{a}}(z)}{\partial z} + \frac{E_{\mathrm{c}}(r_{\mathrm{c}}^2 - r_{\mathrm{f}}^2)}{E_{\mathrm{f}} r_{\mathrm{f}}^2} \cdot \frac{\partial \bar{\varepsilon}_z^{\mathrm{c}}(z)}{\partial z} + \frac{\partial \bar{\varepsilon}_z^{\mathrm{f}}(z)}{\partial z} \right]. \tag{4}$$

As the stiffnesses of the host material, adhesive layer and protective coating are two orders less than that of the fibre core [6], equation (4) becomes

$$\tau_{rz}^{\mathrm{m}}(r, z) \approx -\frac{E_{\mathrm{f}} r_{\mathrm{f}}^2}{2r} \left[\frac{\mathrm{d}\bar{\varepsilon}_z^{\mathrm{f}}(z)}{\mathrm{d}z} \right]. \tag{5}$$

The shear stress is then expressed in terms of the shear modulus of the host material (G_{m}) and material displacements in the w-direction only since u-displacements caused by the Poisson
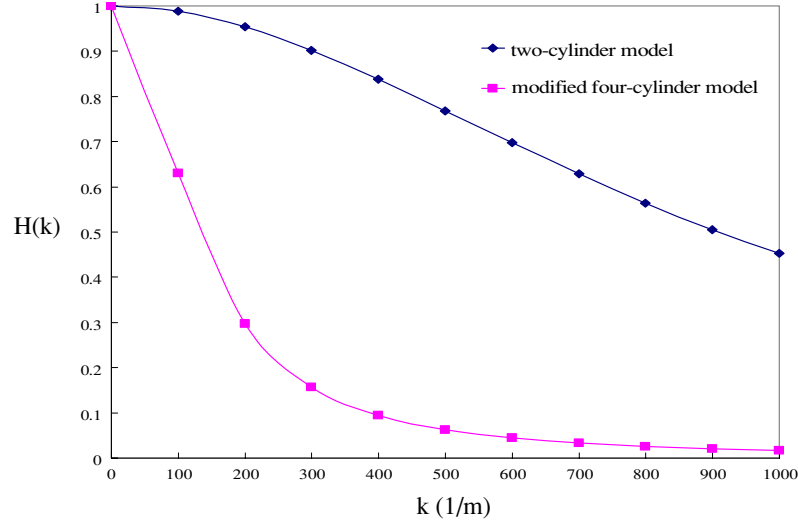
Figure 5. Transfer function of the system against k.

contraction are less significant than w-displacements as

$$\tau_{rz}^{\mathrm{m}}(r, z) = G_{\mathrm{m}} \left[\frac{\partial w^{\mathrm{m}}(r, z)}{\partial r} \right]. \tag{6}$$

Combination of equations (5) and (6) gives

$$\frac{\partial w^{\mathrm{m}}(r, z)}{\partial r} = -\frac{E_{\mathrm{f}}}{E_{\mathrm{m}}} (1 + \nu_{\mathrm{m}}) r_{\mathrm{f}}^2 \frac{\partial \bar{\varepsilon}_z^{\mathrm{f}}(z)}{\partial z}. \tag{7}$$

Integrating both sides of equation (7) with respect to r yields

$$w^{\mathrm{m}}(r_{\mathrm{m}}, z) - w^{\mathrm{m}}(r_{\mathrm{a}}, z) = -\frac{E_{\mathrm{f}}}{E_{\mathrm{m}}} (1 + \nu_{\mathrm{m}}) r_{\mathrm{f}}^2 \ln\left(\frac{r_{\mathrm{m}}}{r_{\mathrm{a}}}\right) \frac{\partial \bar{\varepsilon}_z^{\mathrm{f}}(z)}{\partial z}. \tag{8}$$

Since the axial displacement of the host material can be obtained by considering the condition of compatibility for all elements,

$$w^{\mathrm{m}}(r_{\mathrm{a}}, z) = \delta_{\mathrm{a}}(z) + \delta_{\mathrm{c}}(z) + w^{\mathrm{f}}(r_{\mathrm{f}}, z), \tag{9}$$

in which the relative displacements of the adhesive layer and the protective coating are determined by

$$\delta_{\mathrm{a}}(z) = \frac{1}{G_{\mathrm{a}}} \int_{r_{\mathrm{c}}}^{r_{\mathrm{a}}} \tau_{rz}(r, z) \, \mathrm{d}r \tag{10a}$$

and

$$\delta_{\mathrm{c}}(z) = \frac{1}{G_{\mathrm{c}}} \int_{r_{\mathrm{f}}}^{r_{\mathrm{c}}} \tau_{rz}(r, z) \, \mathrm{d}r. \tag{10b}$$

Substituting equation (10) into equation (9) and equating equation (8),

$$\left(\frac{r_{\mathrm{f}}}{n}\right)^2 \frac{\partial^2 \bar{\varepsilon}_z^{\mathrm{f}}(z)}{\partial z^2} - \bar{\varepsilon}_z^{\mathrm{f}}(z) = -\bar{\varepsilon}_z^{\mathrm{m}}(r_{\mathrm{f}}, z), \tag{11}$$

where n is the shear–lag parameter which encapsulates both the effects of geometry and the relative stiffness of the system components and is written as

$$n^2 = \frac{1}{\frac{E_{\mathrm{f}} r_{\mathrm{c}}}{2 r_{\mathrm{a}}} \left(\frac{1}{G_{\mathrm{a}}} \ln\left(\frac{r_{\mathrm{a}}}{r_{\mathrm{c}}}\right) + \frac{1}{G_{\mathrm{c}}} \ln\left(\frac{r_{\mathrm{c}}}{r_{\mathrm{f}}}\right) \right) + \frac{E_{\mathrm{f}}}{E_{\mathrm{m}}} (1 + \nu_{\mathrm{m}}) \ln\left(\frac{r_{\mathrm{m}}}{r_{\mathrm{a}}}\right)}. \tag{12}$$

Equation (11) is a second-order, inhomogeneous, linear differential equation with the in-fibre strain, $\bar{\varepsilon}_z^{\mathrm{f}}(z)$, sought as a function of the axial coordinate, z. The inhomogeneous term, $\bar{\varepsilon}_z^{\mathrm{m}}(r_{\mathrm{m}}, z)$, is a forcing function, at r_{m}, that drives the response

Table 1. Mechanical and geometrical properties of the optical fibre embedded system.

Description	Symbols	Values
Radius of bare fibre (μm)	r_{f}	62.5
Outer radius of protective coating (μm)	r_{c}	125
Thickness of adhesive layer (mm)	t_{a}	0.1
Thickness of glass fibre composite (mm)	t_{m}	0.2
Young's modulus (GPa)		
Bare fibre	E_{f}	72
Protective coating	E_{c}	0.1
Adhesive material	E_{a}	3.3
Glass fibre composite	E_{m}	15
Shear modulus (GPa)		
Protective coating	G_{c}	0.037
Adhesive material	G_{a}	1.2
Glass fibre composite	G_{m}	6.5789

of the in-fibre strain, $\bar{\varepsilon}_z^{\mathrm{f}}(z)$. Equation (11) is the same as the standard shear–lag relationship, except that $\bar{\varepsilon}_z^{\mathrm{m}}(r_{\mathrm{m}}, z)$ now varies with z. The shear–lag parameter (n) in the case of the two-cylinder model is as follows [6]:

$$n^2 = \frac{E_{\mathrm{m}}}{E_{\mathrm{f}}} \cdot \frac{1}{(1 + \nu_{\mathrm{m}}) \ln(r_{\mathrm{m}}/r_{\mathrm{f}})}. \tag{13}$$

Equation (11) is solved by the Fourier transform followed by the steps addressed in Duck and LeBlanc's model [6], in which the transfer function of the system is defined as

$$H(k) = \frac{\hat{\varepsilon}_z^{\mathrm{f}}(k)}{\hat{\varepsilon}_z^{\mathrm{m}}(r_{\mathrm{m}}, k)} = \frac{1}{(2\pi k r_{\mathrm{f}}/n)^2 + 1}. \tag{14}$$

In this study, a typical singly periodic function (i.e. $\bar{\varepsilon}_z^{\mathrm{m}}(r_{\mathrm{m}}, z) = \cos(2\pi k z)$) with different k was assumed to be applied on the surface of the host material for simulating the induced strain field in the fibre core $\left(\bar{\varepsilon}_z^{\mathrm{f}}(z)\right)$. Table 1 lists the material and geometrical properties of the optical fibre embedded system. By using this table, $H(k)$ can be calculated. Figure 5 indicates the transfer function $H(k)$ with different values of k in the cases of two-cylinder and modified four-cylinder models. The higher k means a more abrupt strain variation applied on the surface of the host material. The transfer function generally
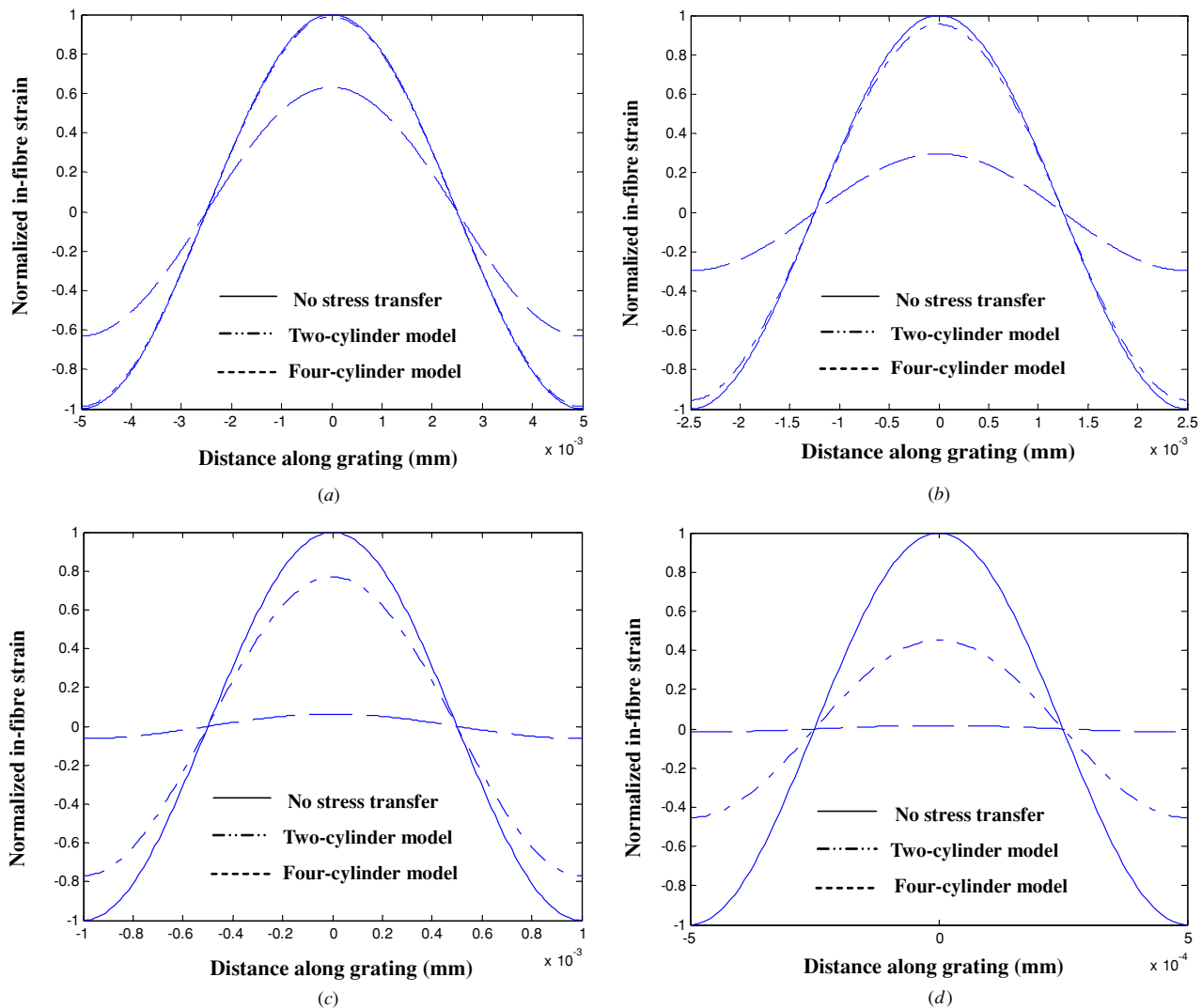
Figure 6. Transfer of a single period of function $\varepsilon_z^m(r_m, z) = \cos(2\pi kz)$ with (*a*) $k = 100$, (*b*) $k = 200$, (*c*) $k = 500$ and (*d*) $k = 1000$.

decreases with increasing k in both cases. This implies that the efficiency of the strain transfer from the host material to the bare fibre strongly depends on the shape of the applied strain distribution. The transfer function gradually drops with increasing k for the two-cylinder model, while it decreases in an exponential manner with increasing k for the modified four-cylinder model. It is reasonable to obtain these results as the strain attenuation should be greater for transferring strain through four material layers in the modified four-cylinder model rather than the two-cylinder model with two material layers only.

The applied strain profile at the surface of the host material and the induced strain distributions at the bare fibre obtained from the two-cylinder and modified four-cylinder models, but with different values of k, are illustrated in figures 6(*a*)–(*d*). Both shape and amplitude of the strain profile are changed after the strain transfer. The higher the k, the weaker the strain transfer obtained. It is important to note that the reflection spectrum from the FBG sensor cannot be simulated accurately without knowing the in-fibre strain distribution obtained by the modified four-cylinder model.

3.2. FEM model

A FEM analysis, using a MSC visual Nastran/Patran commercial software package, was carried out to calculate the surface strain distribution at the grating region while a glass fibre–reinforced epoxy (GF/EP) composite beam was subjected to a three-point bending load. It is generally assumed that the material properties are constant in the width-wise direction for an isotropic material. A 2D FE model, depicted graphically in figure 7, was chosen to simulate the beam under a three-point bending test in the present study. Moreover, the effects of the embedded optical fibre are neglected here although these effects cannot be ignored under some conditions [15]. The mesh was generated using six-noded triangular finite elements. Two-way bias elements, as emphasized in figure 7, were selected in a region near the gauge length to achieve a high resolution of strain variation. There are 7982 nodes and 3401 elements in this model. Linear elastic properties of GF/EP composite were assumed. The elastic modulus and the Poisson ratio of GF/EP composite are 15 GPa m^{-2} and 0.14, respectively. The surface strain
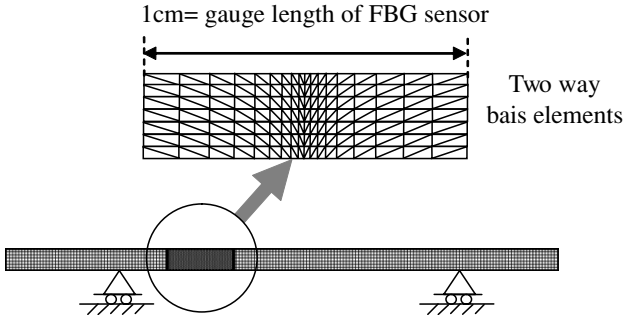
Figure 7. A FEM for a beam under a three-point bending test.
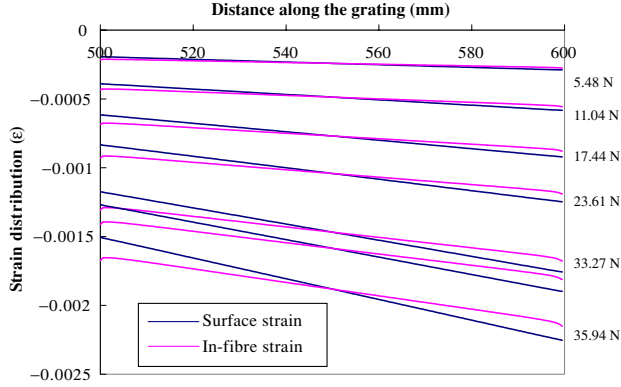
Figure 8. Surface and in-fibre strain distributions at the grating region of GF/EP beam with various applied loads based on the FEM calculation and the modified four-cylinder model.

distribution within the grating region can then be obtained at every 5 mm lateral displacement of the loading head.

The surface strain distribution within the grating region when the beam was loaded with various bending loads based on a FEM calculation is exhibited in figure 8. The beam exhibited a linear strain gradient while it was subjected to the bending loads and the strain gradient increases with the increasing applied load under this loading condition. This figure also shows the in-fibre strain distribution, which was calculated by means of the modified four-cylinder model based on the corresponding surface strain distribution obtained from the FEM analysis. Obviously, the strain gradient of the in-fibre strain distribution is smaller than that of the surface strain distribution and a reduction of the strain gradient increases with the increasing bending load. Furthermore, the average strain values of the surface and the in-fibre strains remain the same.

3.3. Spectrum simulation

A FBG is defined as a small periodical perturbation to the effective index of refraction n_{eff} of an optical fibre core described by [16]

$$\delta n_{\text{eff}}(z) = \overline{\delta n_{\text{eff}}} \left\{ 1 + \nu \cos \left[\frac{2\pi}{\Lambda_0} z + \phi(z) \right] \right\}, \quad (15)$$

where ν is the fringe visibility, Λ_0 is the nominal period, $\phi(z)$ is the grating chirp and $\overline{\delta n_{\text{eff}}}$ is the 'dc' index change spatially averaged over a grating period. By coupled-mode theory, the

first-order differential equations describing mode propagation through the grating in the z-direction are

$$\frac{dR(z)}{dz} = i\hat{\sigma} R(z) + i\kappa S(z) \quad (16a)$$

and

$$\frac{dS(z)}{dz} = -i\hat{\sigma} S(z) - i\kappa R(z), \quad (16b)$$

where $R(z)$ and $S(z)$ are the amplitudes of the forward- and backward-propagating modes, respectively. $\hat{\sigma}$ is the general 'dc' self-coupling coefficient as a function of the propagating wavelength λ, defined as

$$\hat{\sigma} = 2\pi n_{\text{eff}} \left(\frac{1}{\lambda} - \frac{1}{\lambda_D} \right) + \frac{2\pi}{\lambda} \overline{\delta n_{\text{eff}}} - \frac{1}{2} \phi'(z), \quad (17)$$

where $\phi'(z) = d\phi/dz$ and $\phi'(z) = 0$ for the uniform grating, $\lambda_D = 2 n_{\text{eff}} \Lambda_0$ is the designed wavelength (1540.2 nm in this study) and $\kappa = \frac{\pi}{\lambda} \nu \overline{\delta n_{\text{eff}}}$ is the 'ac' coupling coefficient, in which $\overline{\delta n_{\text{eff}}} = 1.131 \times 10^{-4}$ and $\nu \approx 1$.

The length of a uniform grating is assumed to be L ($L = 10$ mm), so the limit of the grating is defined as $-L/2 \leqslant z \leqslant L/2$, while the boundary conditions of the uniform Bragg grating are $R(-L/2) = 1$ and $S(L/2) = 0$ [16]. The reflectivity of the Bragg grating, calculated as a function of the wavelength, can be expressed as

$$r(\lambda) = \left| \frac{S(-L/2)}{R(-L/2)} \right|^2. \quad (18)$$

To obtain the reflectivity of the uniform Bragg grating, which is subjected to either uniform or non-uniform strain, the T-matrix formulation is used to model the Bragg grating with non-constant properties. In this approach, the grating is assumed to be divided into M small sections, each with uniform coupling properties. It is important to note that M cannot be arbitrarily large since several grating periods are required for complete coupling. Hence, M is constrained as [3]

$$M \ll \frac{2 n_{\text{eff}} L}{\lambda_D}, \quad (19)$$

and M is set to be 200 in the present study.

By defining R_i and S_i as the field amplitudes after traversing the ith grating section, the propagation through this uniform section can be described by

$$\begin{bmatrix} R_i \\ S_i \end{bmatrix} = F_i \begin{bmatrix} R_{i-1} \\ S_{i-1} \end{bmatrix}, \quad (20)$$

where

$$F_i = \begin{bmatrix} \cosh(\gamma_B \Delta z) - i\frac{\hat{\sigma}}{\gamma_B} \sinh(\gamma_B \Delta z) & -i\frac{\kappa}{\gamma_B} \sinh(\gamma_B \Delta z) \\ i\frac{\kappa}{\gamma_B} \sinh(\gamma_B \Delta z) & \cosh(\gamma_B \Delta z) + i\frac{\hat{\sigma}}{\gamma_B} \sinh(\gamma_B \Delta z) \end{bmatrix},$$

in which Δz is the length of each section and $\gamma_B = \sqrt{\kappa^2 - \hat{\sigma}^2}$. As a result, the T-matrix formulation for entire grating can be written as

$$\begin{bmatrix} R(-L/2) \\ S(-L/2) \end{bmatrix} = F \begin{bmatrix} R(L/2) \\ S(L/2) \end{bmatrix}, \quad (21)$$
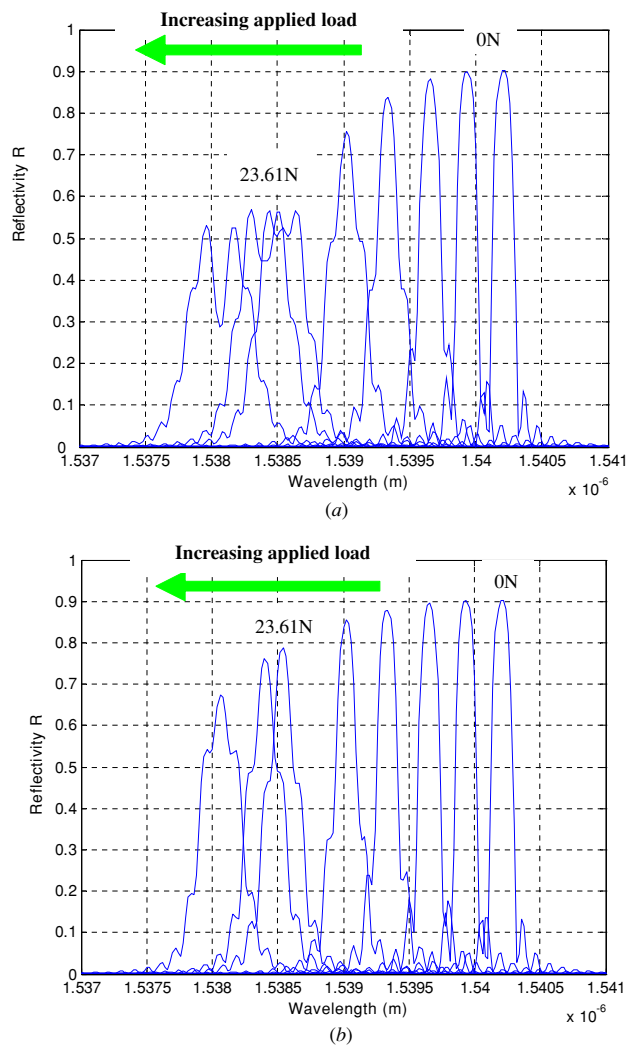
Figure 9. (*a*) Simulated reflection spectra from the FBG sensor based on the surface strain distribution along the grating obtained from the FEM. (*b*) Simulated reflection spectra from the FBG sensor based on the in-fibre strain distribution along the grating obtained from the FEM with the consideration of the stress transfer model.

where $F = F_M \cdot F_{M-1} \cdots F_1$. The reflectivity of the entire grating is then calculated using equation (18).

By using the above FEM results, the reflection spectra from the FBG sensor in which the specimen was loaded with various bending loads can be simulated in virtue of the T-matrix formulation. Such reflection spectra simulated based on the surface and the in-fibre strain distributions are illustrated in figures 9(*a*) and (*b*), respectively.

For the cases of the reflection spectra obtained from the surface and the in-fibre strain distributions, as illustrated in figures 9(*a*) and (*b*), the level of intensity and the bandwidth of the reflection spectrum decreases and increases with the increasing load, respectively. These changes can be explained by the properties of the uniform FBG subjected to the linear strain gradient. The chirped grating effect [3] occurs when the uniform FBG exhibits the linear strain gradient. The level of strain gradients in different loading cases can be found in figure 8. Moreover, a shift of single peak to smaller wavelength results from the FBG sensor subjected to a compressive strain
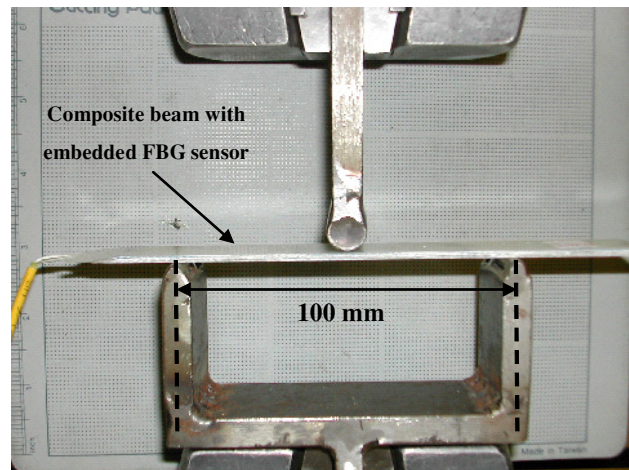
Figure 10. Three-point bending test configuration.

during the bending test. The single peak starts to distort when the applied load is larger than approximately 18 N in the case of the surface strain distribution. However, such a distortion does not occur in the case of the reflection spectra simulated based on the in-fibre strain distribution. Referring to the FEM results in figure 8, the distortion found in the spectrum can be explained by the level of strain gradient. The higher the strain gradient, the higher the chance for a spectrum distortion to occur. This figure clearly demonstrated a correlation of the strain distribution along the grating and the reflection spectrum. Even for the same average strain, the form of the reflection spectrum is totally different since the shape of the strain profile along the grating is not the same.

3.4. Experimental validation

In this experiment, a GF/EP composite beam (16 cm × 2.5 cm × 0.2 cm), with the mechanical properties of $E_{11} = E_{22} = 13.363$ GPa, $G_{12} = 5.86$ GPa, $\nu = 0.14$ and $\rho = 1664.03$ kg m^{-3}, was fabricated by a hand lay-up process for conducting a three-point bending test. Figure 10 depicts a photograph of the three-point bending test configuration. The test was processed using an MTS static axial loading test machine. The specimen was loaded under a constant displacement rate of 0.5 mm min^{-1}. The strain distribution along the grating was recorded by the FBG sensor as illustrated in a form of the reflection spectrum which was displayed in an optical spectrum analyser and then saved in every extension interval with 0.5 mm instantaneously. The test was stopped when the extension reached 3.5 mm. A schematic diagram of a whole data acquisition system in this experiment is indicated in figure 11.

The experimental results of the reflection spectra obtained from the FBG sensor are shown in figure 12. There is no observable distortion of the reflection spectrum obtained from the experiment. Such an observation exhibits good agreement with the simulation found in figure 9(*b*), in terms of the shape, the level of intensity as well as the Bragg wavelength shift. However, the discrepancy in the shape of the reflection spectrum is noted in the case of the simulated spectra in the presence of the strain distribution without the strain transformation, as indicated in figure 9(*a*). These
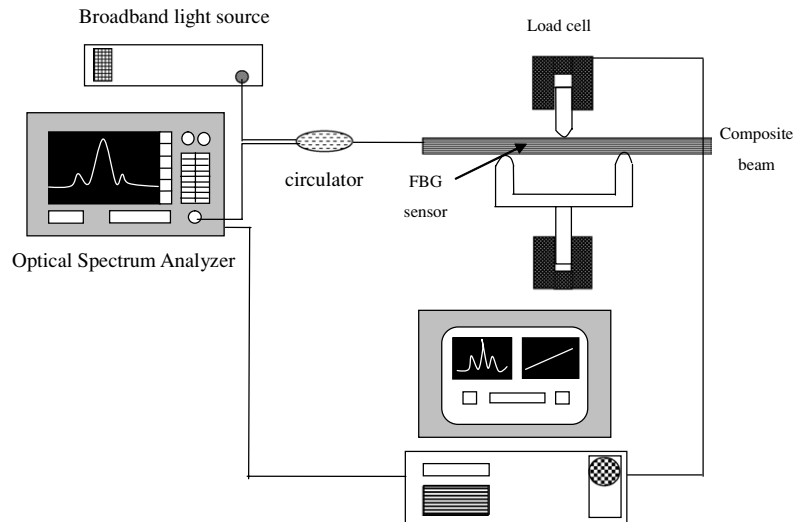
Figure 11. A schematic diagram of a whole data acquisition system for a three-point bending test.
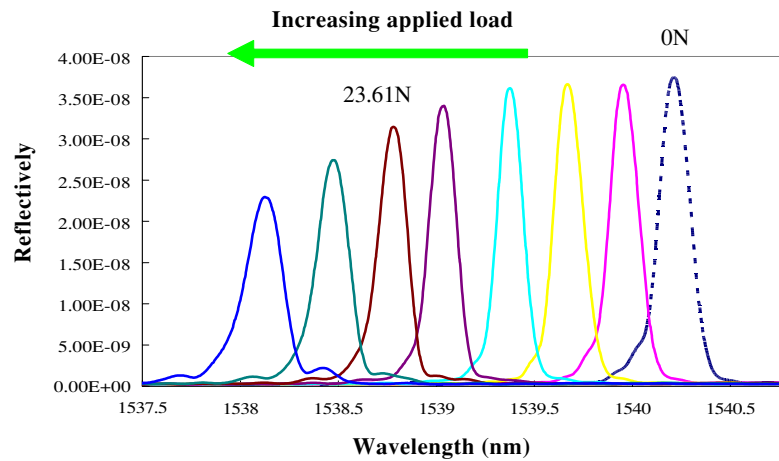
Figure 12. Reflection spectra captured from the FBG sensor during a three-point bending test.

results imply that the change in the shape of the strain profile due to the existence of the protective coating and the adhesive layer significantly affects the reflection spectrum from the FBG sensor. This influence becomes more obvious when the strain gradient along the grating is higher. Therefore, the response of the FBG sensor can only be simulated accurately in conjunction with the modified four-cylinder strain transfer model. Without the deployment of such a transfer model, the response of the FBG sensor would be overestimated, and hence, result in the distortion of the reflection spectrum

4. Conclusion

This paper presents the methodology for evaluating the response of embedded FBG sensors in a composite structure based on the non-uniform strain found in a host material. By virtue of the strain transfer mechanism of the optical fibre embedded structure, FEM analysis and T-matrix formulation, the reflection spectra from the embedded FBG sensor which was subjected to various bending loads were estimated on the

basis of the in-fibre strain distribution. From the experimental validation, the reflection spectra captured from the OSA in the bending test were in good agreement with those obtained by the spectrum simulation based on the in-fibre strain distribution, in terms of the spectrum parameters such as the shape, the level of intensity and the Bragg wavelength shift. However, the discrepancy was found in the case of the simulative spectra obtained from the surface strain in the host material for which the distortion of the reflection spectrum was observed. Such a result demonstrates the importance of the strain transfer mechanism to the accuracy of the reflection spectrum construction.

In practice, the damage in the composite structures can be detected by the FBG sensor since the non-uniform strain caused by the damage may give the failure threshold of the structures. Such a damage detection scheme can be developed provided that the relationship between the in-fibre strain field along the grating and the reflection spectrum is well defined. The proposed method can effectively establish this relationship assisted by the theoretical or the numerical model of the damaged structures. Future works will focus on the reconstruction of the reflection spectrum from the

embedded FBG sensors in delaminated composite structures using the methodology presented in this paper. By knowing the correlation of the in-fibre strain distribution somewhere near the delamination and the simulated reflection spectrum, the delamination location, probably its size, can be identified in association with some inverse problem techniques to be solved.

Acknowledgment

References

[1] Rao Y J 1998 Fibre Bragg grating sensors: principles and applications *Optical Fibre Sensor Technology* vol 2 ed K T V Grattan and B T Maggitt (London: Chapman and Hall) pp 355–89

[2] Rao Y J 1999 Recent progress in applications of in-fibre Bragg grating sensors *Opt. Lasers Eng.* **31** 297–324

[3] Peters K, Studer M, Botsis J, Iocco A, Limberger H and Salathe R 2001 Embedded optical fibre Bragg grating sensor in a nonuniform strain field: measurements and simulations *Exp. Mech.* **41** 19–28

[4] Kim K S, Kollar L and Springer G S 1993 A model of embedded fibre optic Fabry–Perot temperature and strain sensors *J. Compos. Mater.* **27** 1618–62

[5] Duck G, Renaud G and Measures R 1999 The mechanical load transfer into a distributed optical fibre sensor due to a linear strain gradient: embedded and surface bonded cases *Smart Mater. Struct.* **8** 175–81

[6] Duck G and LeBlanc M 2000 Arbitrary strain transfer from a host to an embedded fibre-optic sensor *Smart Mater. Struct.* **9** 492–7

[7] Lau K T, Yuan L, Zhou L, Wu J and Woo C 2001 Strain monitoring in FRP laminates and concrete beams using FBG sensors *Compos. Struct.* **51** 9–20

[8] Ling H Y, Lau K T and Cheng L 2004 Determination of dynamic stress profile of composite structures using embedded multiplexed fibre-optic sensors *Compos. Struct.* **66** 317–26

[9] Huang S, LeBlanc M, Ohn M M and Measures R M 1995 Bragg intragrating structural sensing *Appl. Opt.* **34** 5003–9

[10] Tamada M and Sakuda K 1987 Analysis of almost-periodic distributed feedback slab waveguides via a fundamental matrix approach *Appl. Opt.* **26** 3474–8

[11] Peters K, Pattis P, Botsis J and Giaccari P 2000 Experimental verification of response of embedded optical fibre Bragg grating sensors in non-homogenous strain fields *Opt. Lasers Eng.* **33** 107–19

[12] Prabhugoud M and Peters K 2004 Modified transfer matrix formulation for Bragg grating strain sensors *J. Lightwave Technol.* **22** 2302–9

[13] Rao Y J 1997 In-fibre Bragg grating sensors *Meas. Sci. Technol.* **8** 355–75

[14] Measures R M 1992 Smart composite structures with embedded sensors *Compos. Eng.* **2** 597–618

[15] Ling H Y, Lau K T and Lam C K 2005 Effects of embedded optical fibre on mode II fracture behaviours of woven composite laminates *Composites* B **36** 534–43

[16] Hill K O and Meltz G 1997 Fibre Bragg grating technology fundamentals and overview *J. Lightwave Technol.* **15** 1263–76